Analysis and comparison of heat flux of landfast ice during 2016 in the Prydz Bay, Antarctica

Guanghua Hao[1], Jie Su[2, 3*], Qinghua Yang[4, 5], Long Lin[6], Shutao Cao[2, 3]

[1] Key Laboratory of Marine Hazards Forecasting, National Marine Environmental Forecasting Center, Ministry of Natural Resources, Beijing 100081, China

[2] Physical Oceanography Laboratory, Ocean University of China, Qingdao 266100, China

[3] Pilot National Laboratory for Marine Science and Technology (Qingdao), Qingdao 266237, China

[4] School of Atmospheric Sciences, Sun Yat-sen University, Guangzhou 510275, China

[5] Southern Marine Science and Engineering Guangdong Laboratory (Zhuhai), Zhuhai 519080, China

[6] Second Institute of Oceanography, Ministry of Natural Resources, Hangzhou 310012, China

© Chinese Society for Oceanography and Springer-Verlag GmbH Germany, part of Springer Nature 2021

Abstract

Long term *in situ* atmospheric observation of the landfast ice nearby Zhongshan Station in the Prydz Bay was performed from April to November 2016. The *in situ* observation, including the conventional meteorological elements and turbulent flux, enabled this study to evaluate the sea ice surface energy budget process. Using *in situ* observations, three different reanalysis datasets from the European Centre for Medium-Range Weather Forecasts Interim Re-analysis (ERA-Interim), National Centers for Environmental Prediction Reanalysis2 (NCEP R2), and Japanese 55-year Reanalysis (JRA55), and the Los Alamos sea ice model, CICE, output for surface fluxes were evaluated. The observed sensible heat flux (*SH*) and net longwave radiation showed seasonal variation with increasing temperature. Air temperature rose from the middle of October as the solar elevation angle increased. The ice surface lost more energy by outgoing longwave radiation as temperature increased, while the shortwave radiation showed obvious increases from the middle of October. The oceanic heat flux demonstrated seasonal variation and decreased with time, where the average values were 21 W/m² and 11 W/m², before and after August, respectively. The comparisons with *in situ* observations show that, *SH* and *LE* (latent heat flux) of JRA55 dataset had the smallest bias and mean absolute error (MAE), and those of NCEP R2 data show the largest differences. The ERA-Interim dataset had the highest spatial resolution, but performance was modest with bias and MAE between JRA55 and NCEP R2 compare with *in situ* observation. The CICE results (*SH* and *LE*) were consistent with the observed data but did not demonstrate the amplitude of inner seasonal variation. The comparison revealed better shortwave and longwave radiation stimulation based on the ERA-Interim forcing in CICE than the radiation of ERA-Interim. The average sea ice temperature decreased in June and July and increased after September, which was similar to the temperature measured by buoys, with a bias and MAE of 0.9°C and 1.0°C, respectively.

Key words: energy flux, *in situ* observation, evaluation, CICE 6, reanalysis data

---

1 Introduction

Sea ice is an important component in the climate system, which strongly affects the energy balance through the ice albedo feedback mechanism (Elders and Pegion, 2017). The Antarctic sea ice cover has a strong influence on the atmosphere and ocean (Valkonen et al., 2008). A previous study showed the sea ice extent increased with a rate of 1.7% per decade during the 1979–2015 period (Comiso et al., 2017), but the sea ice cover began to decrease in 2014. In the Antarctic, the sea ice is on average thinner, at lower concentration and, is located at lower latitudes than in the Arctic, and is often impacted by the katabatic winds from cold continental areas (Vihma et al., 2009), such as Zhongshan Station, which was affected by the overnight katabatic winds almost every day.

The change of sea ice cover will affect the surface energy flux. Surface energy balance is important to the interaction between the ocean and the atmosphere, which also affects the formation and ablation of the sea ice (Wendler and Worby, 2001). The surface energy balance includes radiative fluxes, turbulent heat fluxes, which have been carried out in the polar regions to learn about its climate processes (Perovich et al., 2002; Persson et al., 2002; Perovich and Polashenski, 2012; Walden et al., 2017; Yu et al., 2017). However, it was difficult to accurately estimate the local turbulent surface flux due to the lack of observations.

Direct observations of surface turbulent and radiative flux measurements over sea ice have rarely been conducted, especially in the Antarctic (Allison et al., 1982; Wendler et al., 1997; Wendler and Worby, 2001; Vihma et al., 2009; Van Den Broeke et

al., 2005), although several studies have investigated the variability of surface radiation fluxes over the Antarctic land surface (Välisuo et al., 2014; King et al., 2015; Yang et al., 2016). Liu et al. (2020) found that the strong winds in the katabatic wind zone enhance the downward sensible heat flux (*SH*) in Antarctica. The limited observations have resulted in most surface energy budgets over Antarctic sea ice having been conducted by numerical models (Bintanja and Van Den Broeke, 1995; King et al., 2001). Reanalysis data are widely used in the Antarctic. The European Centre for Medium-Range Weather Forecasts Interim Re-analysis (ERA-Interim), National Centers for Environmental Prediction Reanalysis2 (NCEP R2), and Japanese 55-year Reanalysis (JRA55) datasets cover a long period of time, which is beneficial to research of Antarctica. However, reanalysis data reveals large differences amongst them as well as the *in situ* data (Shu et al., 2012). It is thus worthwhile and imperative to obtain more *in situ* data to improve modeling results. The recent version of the Los Alamos sea ice model (CICE) included the column ice model, which can be used in the study of landfast ice.

The Zhongshan Station is located in the Prydz Bay, East Antarctica, close to the Ice Sheet. The *in situ* observations were gathered at a nearby station. However, the observations and simulations of surface energy balance were sparse, especially for the *in situ* data. The surface energy balance were measured on the Antarctic Plateau (Ding et al., 2019). The diurnal cycle and monthly variation of surface energy balance on landfast ice under the conventional meteorological conditions were analyzed (Liu et al., 2020), which showed the surface energy balance of this region and indicated that latent heat flux (*LE*) and net heat flux (R_n) were balanced by *SH* and ground heat flux (*G*) before October and *LE* was the only surface heat sink. The surface energy balance process is not well represented in current climate models. Thus, observations and model results are both important and necessary for understanding the mechanism of snow/ice among ice, ocean, and atmosphere.

Nonetheless, the reanalysis datasets and model simulations are still important to compare Antarctic sea ice change to *in situ* data, but need to be evaluated by more *in situ* data. In this paper, the data used will be presented in Section 2. In Section 3, this study will first briefly analyze the observation data on the radiative and turbulent surface fluxes over the landfast ice nearby the Zhongshan Station in austral spring to early summer, from 8 April to 26 November 2016. Then, this study will concentrate on the reanalysis data of ERA-Interim, NCEP R2, JRA55, and the CICE output result, which will be evaluated using the observation data in the Zhongshan Station. The discussion and conclusions are drawn in the last section.

2 Data

The Automatic Weather Station (AWS) and buoys were setup at the *in situ* sites. The *in situ* sites were on landfast ice, in the coastal area off the Zhongshan Station (69°22′S, 76°22′E), Prydz Bay, East Antarctica, and were measured continuously from 8 April to 26 November 2016. The observation site was off the nearby islands and free from obstructions in all directions. The AWS includes a series of instruments: the air temperature sensor by probe 107, SI-111, and HMP 155 for both air temperature (T_a), surface temperature (T_s), and humidity. Also there was a three-dimensional sonic anemometer CSAT3B, and an *in situ*, open-path, mid-infrared gas (CO_2/H_2O) analyzer integrated with a 3D sonic anemometer IRGASON, of which more details can be found in Liu et al. (2020). All the data were converted to a daily mean and quality control was carried as described in Liu et al.

(2020). The sea ice temperature and thickness were measured by one nearby sea ice buoy containing 300 temperature sensors, which had temperature sensors per centimeter with a resolution of 0.062 5°C and accuracy of 0.5°C. There were four buoys employed and the one nearest the AWS was used. The calculated sea ice thickness by using buoys with errors of ±7 cm, were evaluated by using the manned drilling hole observed sea ice thickness. The sea ice temperature was also used to calculate the energy exchange between the ice and ocean. The snow depth was manually measured by a stainless-steel ruler every week before 20 September and thereafter almost every day until 26 November, and had an accuracy of 0.1 cm. The cloud fraction was recorded at the Zhongshan (WMO No. 89573) manned weather station, located 1 km inland from the sea ice observation site. The longwave and shortwave radiation were measured by the CNR4 manufactured by Kipp&Zonen (Delft, The Netherlands). The surface turbulent fluxes, *SH* and *LE*, were calculated by a data logger using the eddy covariance method (Blanken et al., 2000).

Reanalysis data (ERA-Interim, NCEP R2, and JRA55) will be evaluated by the *in situ* observation data. ERA-Interim is produced with the observation fields, the forecast model, and a four-dimensional variational assimilation system (4DVAR) with a spectral model integrated (Simmons et al., 2007). The outputs of ERA-Interim were bilinearly interpolated to 10 various resolutions from 0.125° to 3°. The ERA-Interim synoptic of forecast accumulations 8 times per day at the grid resolution of 0.125° were downloaded from the European Center for Medium-Range Weather Forecasts (ECMWF) website. The NCEP R2 dataset provides global reanalysis fields of atmospheric data with a spatial resolution of 1.875° and 4 times per day. NCEP R2 is a second limited version of NCEP-R1 (Kanamitsu et al., 2002). The JRA55 data extended back to 1958 and is the second Japanese global atmospheric reanalysis project. JRA55 also employs 4DVAR data assimilation with a grid resolution of 1.25° (Ebita et al., 2011). The time resolution is 8 times per day. In this study, the daily averaged values of surface *LE*, *SH*, T_a, wind speed, relative humidity, S_{net} (net shortwave radiation) and L_{net} (net longwave radiation), T_s, and cloud fraction from the above three reanalysis datasets were used.

The CICE model, developed by the Los Alamos National Laboratory, USA, is an efficient sea ice component for a fully coupled atmosphere–land–ocean–ice global climate model (Hunke et al., 2018). It is widely used in climate system models due to the complex parameterization. The CICE consists of a thermodynamic component, an ice dynamics component, and a transport component. Displaced-pole grids were used in CICE with a horizontal resolution of 1°×1°, seven ice layers, and one snow layer in the vertical. The numerical experiments in this article are based on CICE version 6. The CICE output results (*SH*, *LE*, upward and downward longwave radiation, downward shortwave radiation, and ice temperature) based on version 6 will also be assessed by using the *in situ* observations. More details can be found in Section 3.3.

3 Results

3.1 *Observation and meteorological conditions*

Daily averaged surface pressure, wind speed, wind direction, cloud cover fraction, T_a, and T_s from 8 April to 26 November 2016 are shown in Fig. 1. According to the statistics reported by a previous study (Liu et al., 2020), the wind speed during the observation period was (4.2±2.3) m/s, and the wind direction was mainly eastern, which can also been seen in Figs 1b and c. It also showed
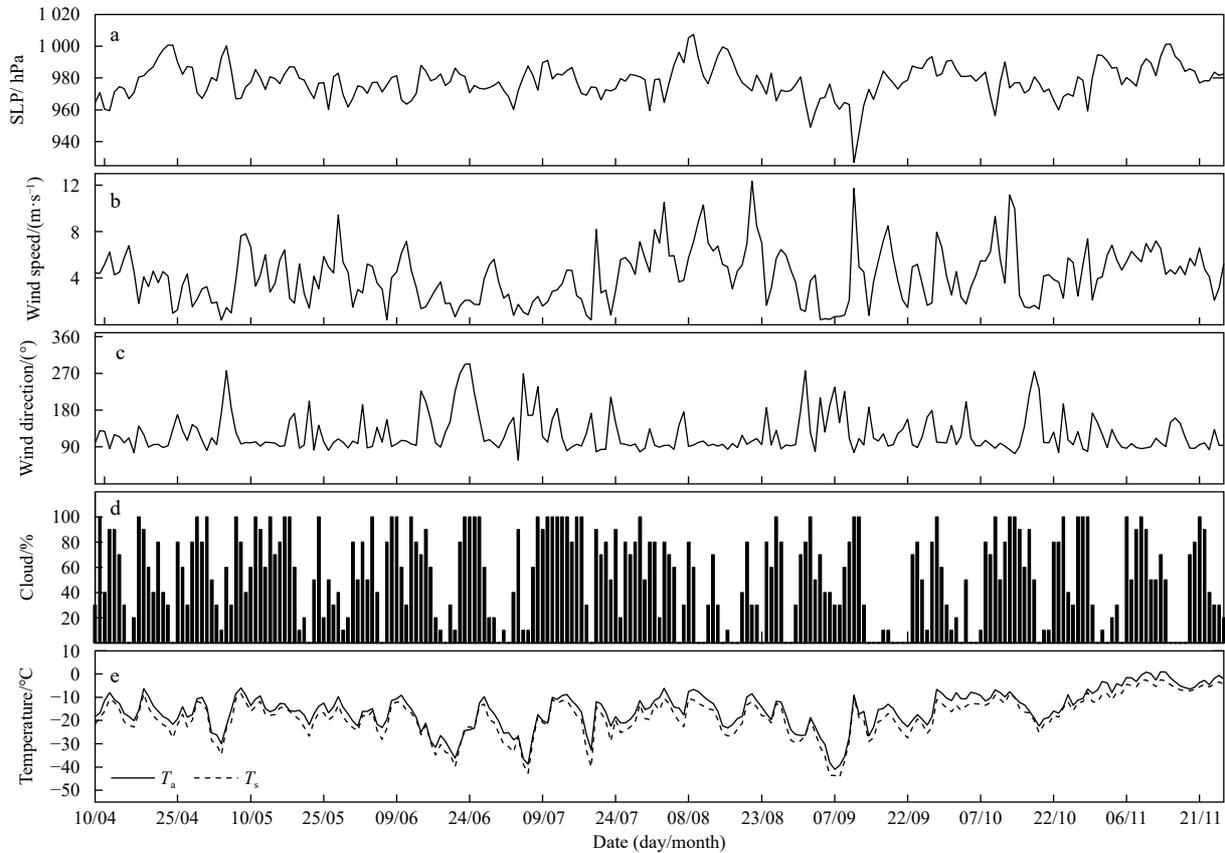
Fig. 1. Daily average sea level pressure (SLP) (a), wind speed (b), wind direction (c), cloud cover fraction (d), and T_a and T_s (e). T_a: air temperature, T_s: surface temperature.

diurnal variation with east-south-easterlies in the morning to east-north-easterlies in the afternoon. The observation site was frequently impacted by a cyclone from the south. In addition to the cyclone, the site was also impacted by katabatic winds from night to early noon, which also contributed to enhancing the diurnal variation of air temperature from the cold katabatic flow from the ice sheet. In this analysis, sea level pressure (SLP) in the Zhongshan Station was measured at (978±10) hPa during 8 April to 26 November 2016 (Fig. 1a). A strong cyclone occurred on 10 September, which fell over 24 hPa within 24 h (the cyclone deepening rate ≥1 hPa/h) and resulted in the largest instantaneous wind speed of 17.5 m/s (daily average wind speed, 11.7 m/s, Fig. 1b). The time series of cloudiness (Fig. 1d) shows 42% of occurrences of clear sky conditions (cloud cover ≤20%) and 45% of occurrences of overcast conditions (cloud cover ≥80%, Fig. 1d), which is similar to the short time (about 2 months) statistical result (Hao et al., 2020). During the observation period, the lowest daily mean T_a at 2 m and T_s were –27.5°C and –30.6°C, respectively (Fig. 1e), and occurred in the first half of September (Fig. 1e). The cyclone caused the air temperature to increase, which continued after the cyclone ended.

3.2 *Assessment of reanalysis data using in situ data*

In this study, the net shortwave radiation flux (S_{net}), net longwave radiation (L_{net}), the surface net radiation (R_n), and the oceanic heat flux F_w (Persson et al., 2002) are determined as

$$S_{net} = S \downarrow - S \uparrow, \qquad (1)$$

$$L_{net} = L \downarrow - L \uparrow, \qquad (2)$$

$$R_n = S_{net} + L_{net}, \qquad (3)$$

where $S \downarrow$, $S \uparrow$, $L \downarrow$, and $L \uparrow$ are the downward shortwave radiation flux, upward shortwave radiation flux, downward longwave radiation flux, and upward longwave radiation flux, respectively. R_n is the sum of S_{net} and L_{net}, which can be partitioned into *LE*, *SH*, and *G* (Zhou and Wang, 2016). In Eqs (1) and (2), a positive S_{net} and L_{net} indicates the surface gains energy.

The environmental parameters (T_s, wind speed, and relative humidity) from the ERA-Interim, NCEP R2, and JRA55 are validated by *in situ* observed data in the Zhongshan Station in this section (Fig. 2). The reanalysis data showed similar seasonal variation as the observation data. The T_a and wind speed of NCEP R2 data showed the largest differences from the observation, with biases of –7.1°C and 7.3°C and mean absolute error (MAE) of 4.2 m/s and 4.3 m/s (Fig. 2a). The result demonstrated the lower air temperature and higher wind speed from the NCEP R2 data than the observation. The bias and MAE among the reanalysis data and the observations are shown in Table 1. The T_a, T_s, and cloud fraction (Figs 2a, d and e) of ERA-Interim showed the least amount of bias and MAE in comparison to the observation data. The wind speed and relative humidity (Figs 2b and c) perform best with the minimum bias and MAE of JRA55. The T_a and T_s also show good agreement with the observation, but they are not better than the result of ERA-Interim. The cloud fraction of JRA55 had the largest bias and MAE. However, it needs stress that the observed cloudiness in the Zhongshan Station was obtained by
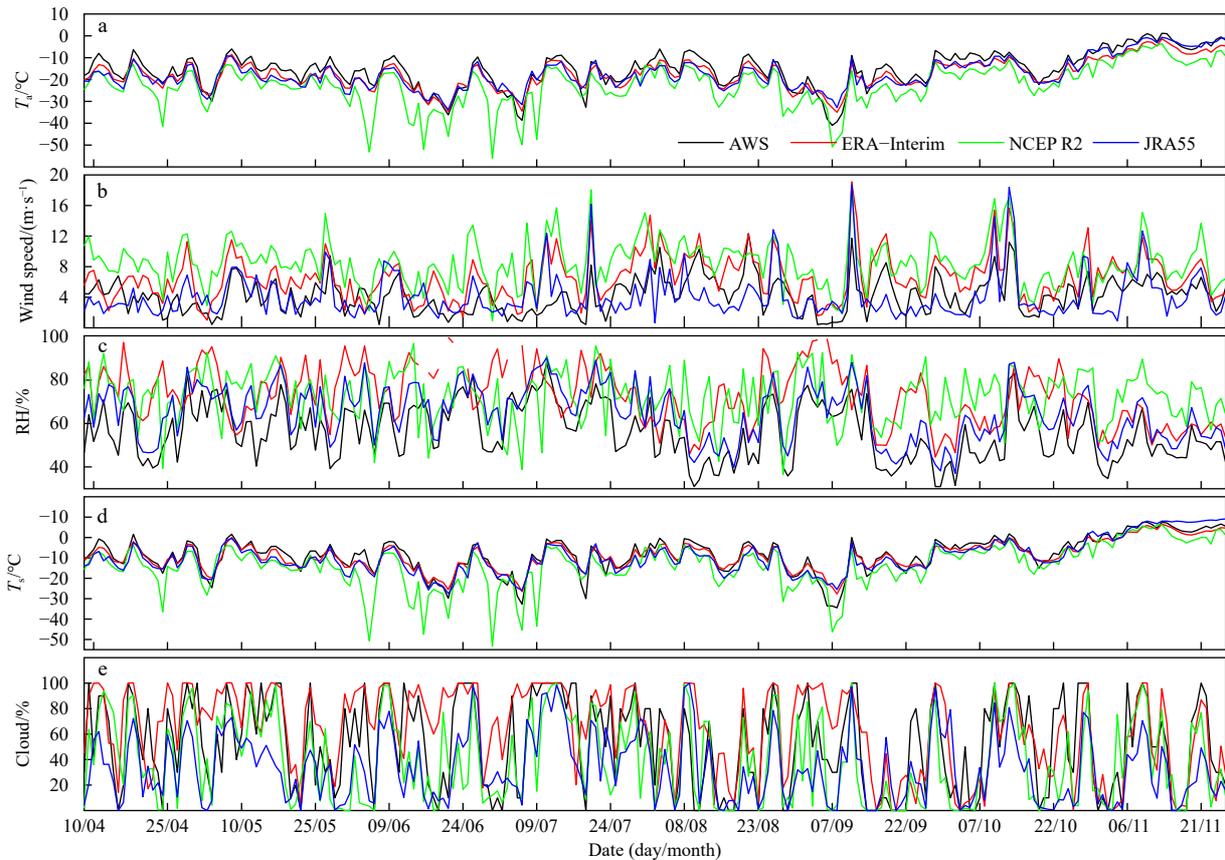
Fig. 2. Daily average T_a (a), wind speed (b), relative humidity (RH) (c), T_s (d), and cloud fraction (e) of *in situ* observations and reanalysis data.

Table 1. The bias and MAE of atmospheric factors between AWS and the reanalysis data

		T_a/°C	WS/(m·s⁻¹)	RH/%	T_s/°C	Cloud/%
ERA-Interim	Bias	−2.1	2.4	16.8	−0.5	10.9
	MAE	2.8	2.5	17.6	1.9	22.6
NCEP R2	Bias	−7.1	4.2	16.2	−5.3	−13.7
	MAE	7.3	4.3	18.5	5.8	21.9
JRA55	Bias	−2.0	−0.1	8.7	−1.3	−19.7
	MAE	3.3	2.1	8.9	2.9	26.0

Note: WS represents wind speed; RH represents relative humidity.

different observers and with subjectivity to some extent. The T_s of NCEP R2 data showed the largest bias and MAE of −5.3°C and 5.8°C and demonstrated larger range during the temperature-fall period than the observed data and the other two datasets (Fig. 2d), which could impact the simulation of outgoing longwave radiation.

Positive *SH* and *LE* indicated sea ice energy gain, as shown in Fig. 3. The surface gained more downward shortwave radiation as the daily noon solar elevation angle increased. According to the statistics reported by Liu et al. (2020), the ice or snow surfaces gain energy from net shortwave radiation flux and *SH*, and they lose energy through *LE* and L_{net}, which is also shown in Fig. 3 during the observation period. The daily mean S_{net} (Fig. 3c) was above zero from the beginning of September and increasing rapidly, which was significant after the polar night and demonstrated seasonal variation caused by the solar elevation angle variation (Fig. 3c). The L_{net} also has shown inner-seasonal vari-

ation and obvious seasonal oscillation of *SH* shown (Fig. 3b), which was mainly caused by the temperature impact of the synoptic process (Fig. 3d). After the middle of October, the L_{net} demonstrated a decreasing trend, which signified more outgoing energy of the surface.

The daily mean turbulent fluxes (*SH* and *LE*) calculated from the *in situ* data and radiation fluxes (S_{net}, L_{net} and R_n; Figs 3c–e) were used to validate those obtained from the three reanalyzed datasets, ERA-Interim, NCEP R2, and JRA55 in the Zhongshan Station, Antarctic. Figure 3 shows that all of the reanalysis data demonstrated the seasonal variation similarly to the observation, except the *SH* of NCEP R2, but still show larger differences for the amplitude.

The *LE* of reanalysis data showed larger differences from the observations from the second half of October, especially for the NCEP R2 data, with melting onset as shown in Fig. 3a. The bias and MAE among the reanalysis data and the observations is shown in Table 2. The *SH* of ERA-Interim and JRA55 show the same fluctuation; however, that of NCEP R2 showed larger differences (Fig. 3b). *SH* of NECP R2 data also showed larger values and bigger variation, with a bias and MAE of 26.1 W/m² and 39.3 W/m². The wind speed also showed bias, which impacted the result of *SH* and *LE*. Before November, the S_{net} of NCEP R2 showed larger differences, and the JRA55 showed larger differences after November. The S_{net} of ERA-Interim data demonstrated more fluctuation compared with other data (Fig. 3c). The L_{net} of ERA-Interim data showed larger negative values than the other datasets, which indicated the surface lost more energy through the thermal radiation process, which may be caused by
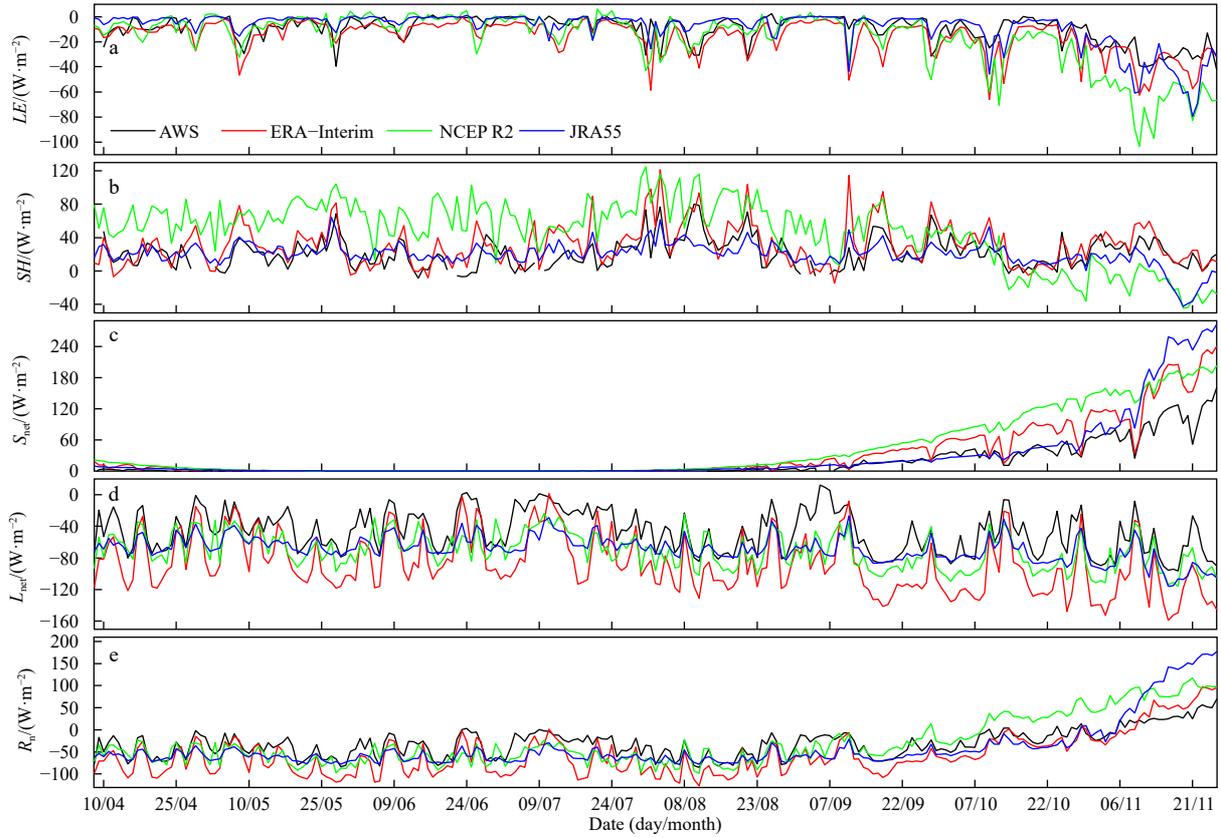
Fig. 3. Daily average LE (a), SH (b), S_{net} (c), L_{net} (d), and R_n (e) of *in situ* observations and reanalysis data.

Table 2. The bias and MAE of flux between AWS and the reanalysis data (unit: W/m²)

		LE	SH	S_{net}	L_{net}	R_n
ERA-Interim	Bias	−6.5	10.2	15.6	−41.2	−25.6
	MAE	7.6	14.3	15.7	41.4	29.7
NCEP R2	Bias	−7.9	26.1	24.8	−24.0	0.8
	MAE	11.3	39.3	24.8	25.7	27.7
JRA55	Bias	0.7	−1.1	12.7	−21.6	−8.9
	MAE	6.8	13.5	13.8	22.1	25.9

the differences in T_s and cloudiness fraction (Fig. 3d). The L_{net} of ERA-Interim shows smaller bias (−41.2 W/m²) than the observations and a larger difference in MAE (41.4 W/m²), which also leads to almost double the difference of R_n than JRA55. The S_{net} also leads to a difference for R_n (Fig. 3e). For the period when shortwave radiation increased due to solar elevation angle increases in the JRA55 and NCEP R2 datasets, the difference of S_{net} also led to a larger difference of R_n. As the positive and negative bias compensated for the overall deviations, the R_n of NCEP R2 demonstrated the smallest bias and larger MAE than JRA55. Among the three reanalysis sets, the JRA55 data showed the smallest differences from the observations in all the variables in the Zhongshan Station.

3.3 *Ocean heat fluxes based on observed ice surface temperature and ice thickness*

Apart from the heat flux exchange between ice and air, the ice also gains energy from the ocean (Fig. 4). The energy budget process (Mcphee and Untersteiner, 1982; Perovich and Elder, 2002;

Lei et al., 2010) is described as follows:

$$F_W = F_C + F_L + F_S, \qquad (4)$$

where F_C is the conductive heat fluxes $\left(F_C = k_{si}\dfrac{\partial T_{si}}{\partial Z_{si}}\right)$ at ice-sea interface, and F_L and F_S are the equivalent latent heat flux $\left(F_L = -\rho_{si}L_f\dfrac{\partial Z_{si}}{\partial t}\right)$ and specific heat flux $\left(F_S = \rho_{si}c_{si}\dfrac{\partial T_{si}}{\partial t}\right)$ in the ice bottom. Additionally, k_{si} is the sea ice thermal conductivity, and $\dfrac{\partial T_{si}}{\partial Z_{si}}$ is the vertical ice temperature gradient. Sea ice density is given by ρ_{si}, L_f is the sea ice latent heat of fusion, $\dfrac{\partial Z_{si}}{\partial t}$ is the ice growth rate, c_{si} is the sea ice specific heat at the basal layer, and $\dfrac{\partial T_{si}}{\partial t}$ is the ice temperature variation rate. The sea ice temperature recorded by the buoy and the calculated sea ice thickness were used to calculated the energy budget process. The oceanic heat flux F_W was calculated using the method described by Lei et al. (2010). The precision of the oceanic heat flux was affected by the ice thickness, temperature, and the specified salinity at the ice base. The positive F_W indicates ice gain energy from the ocean.

The F_C and F_L were the main portions of the ice-ocean energy exchange, which showed opposite signs (Figs 4a and b). The F_S demonstrated small magnitudes and around 0 for the whole period (Fig. 4c). The average F_C, F_L, F_S, and F_W were 27.8 W/m², −12.6 W/m², 0.2 W/m², and 15.4 W/m², respectively, during the evaluated period. The F_W demonstrated obvious seasonal change (Figs 4d and e). Before August, the air temperature decreased and ice thickness increased with the decrease in solar radiance.
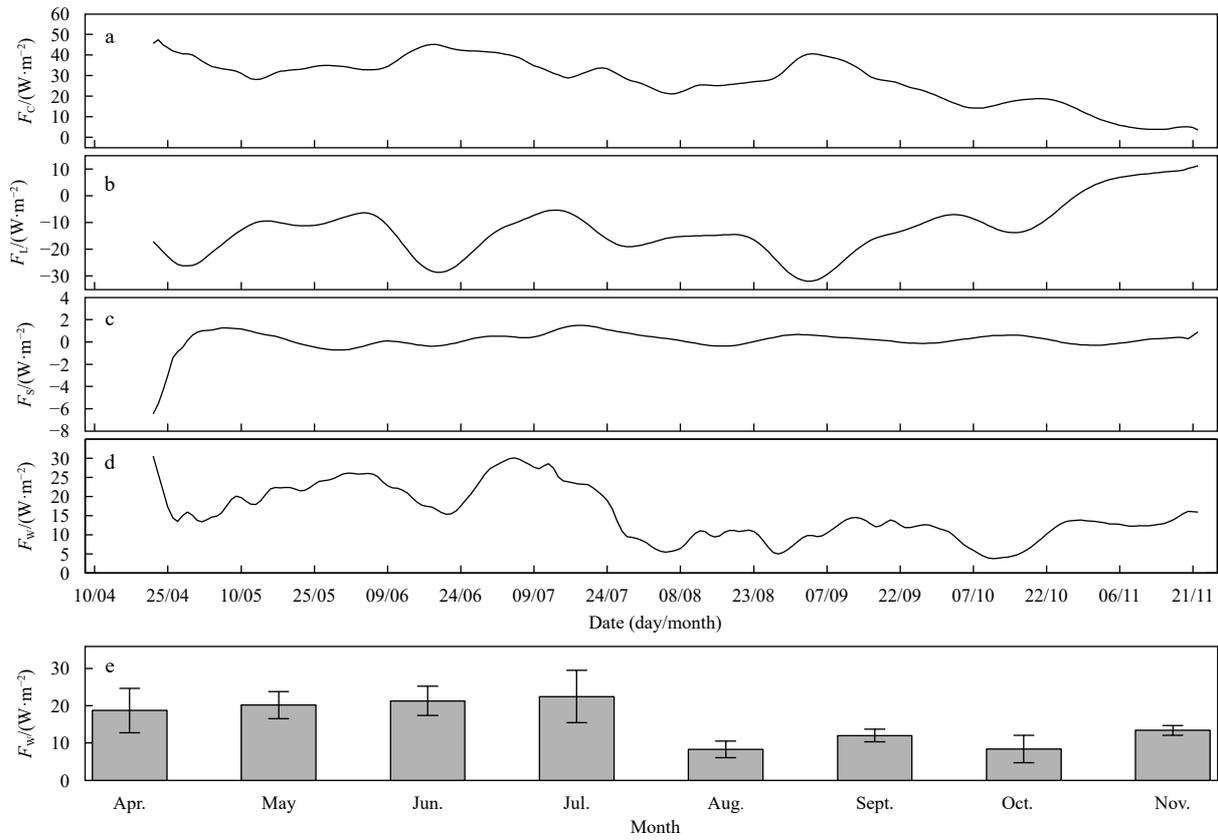
Fig. 4. Conductive heat flux at ice base F_C (a), equivalent latent heat flux F_L (b), specific heat flux F_S (c), oceanic heat flux F_W (d), and monthly mean value of the estimated oceanic heat flux with errors (e). All lines represent a 7-d moving average.

The monthly mean F_W varied within a range of 19–23 W/m² (Fig. 4e), with an average value of 21 W/m². The heat available in the surface ocean reduced from August, with a range from 8 W/m² to 13 W/m², and reached a minimum in August and October, with an average value of 11 W/m², which was consistent with the findings of previous studies (Lei et al., 2010; Zhao et al., 2019), but showed different seasonal variation, which may be due to errors of sea ice thickness measurements derived from the buoys. The calculated F_W was dependent on the sea ice growth rate. The monthly result shows a maximum deviation of ±7 W/m² in July.

3.4 *Comparison with CICE version 6 result*

In this study, the atmospheric force data used ERA-Interim reanalysis data from ECMWF, including wind speed, air temperature, dew-point temperature, precipitation, snowfall, total cloud, SLP, and downward oceanic heat flux. The radiation data were simulated using the ERA-Interim forcing data. The ocean force data were obtained from the Community Climate System Model (CCSM), including the climatological monthly surface tilt, sea surface velocity, heat flux of mixed layer bottom from the output of the CCSM control run and sea surface temperature, and sea surface salinity of Polar science center Hydrographic Climatology (PHC). The integration time was from 1979 to 2016. To compare with the observations at the Zhongshan Station, the nearest grid (69.604 6°S,76.437 5°E) of the CICE output with sea ice thickness more than 0.01 m was chosen from April to November 2016.

The results from CICE version 6 were compared using the ob-

served data at the Zhongshan Station. The results show that the value of *SH* was smaller and *LE* was larger than the observation data. The turbulent heat flux of the CICE (Fig. 5) result demonstrates the smaller range and do not shows the remarkable amplitude of seasonal variation, with *SH* bias and MAE of –21.4 W/m², 22.3 W/m² and *LE* bias and MAE of 3.1 W/m², 5.9 W/m². These results were better than the NCEP R2 compared with the AWS, but showed larger bias than the ERA-Interim. The bias and MAE of *SH* compare with ERA-Interim are –31.1 W/m², –31.2 W/m², and the bias and MAE of *LE* compare with ERA-Interim are 9.4 W/m², 9.5 W/m², which indicated larger turbulence flux than the forcing data. The radiation of the CICE output was calculated by the model parameterized scheme using the forcing data. The upward longwave radiation (Fig. 6a) was consistent with observations. The downward longwave radiation (Fig. 6b) demonstrated seasonal variation, but with a smaller range. The larger difference in downward longwave radiation caused the larger differences of L_{net} (Fig. 6c). The downward shortwave radiation (Fig. 6d) showed an increase with the increase of solar elevation angle, but did not show the variation affected by cloud or synoptic process. The radiation (upward longwave radiation, downward longwave radiation, L_{net}, and downward shortwave radiation) showed bias of 3.9 W/m², 4.7 W/m², 0.8 W/m², and –1.5 W/m² and MAE of 9.4 W/m², 24.0 W/m², 21.6 W/m² and 12.9 W/m² compare with the observations. The radiation shows larger bias of –106.5 W/m², –64.7 W/m², 41.8 W/m², and –40.0 W/m², and MAE of 106.5 W/m², 64.7 W/m², 46.6 W/m² and 43.4 W/m² with the ERA-Interim data, which indicated the better stimulation of radiation in CICE than the ERA-Interim radiation. The L_{net} of CICE does not show a large
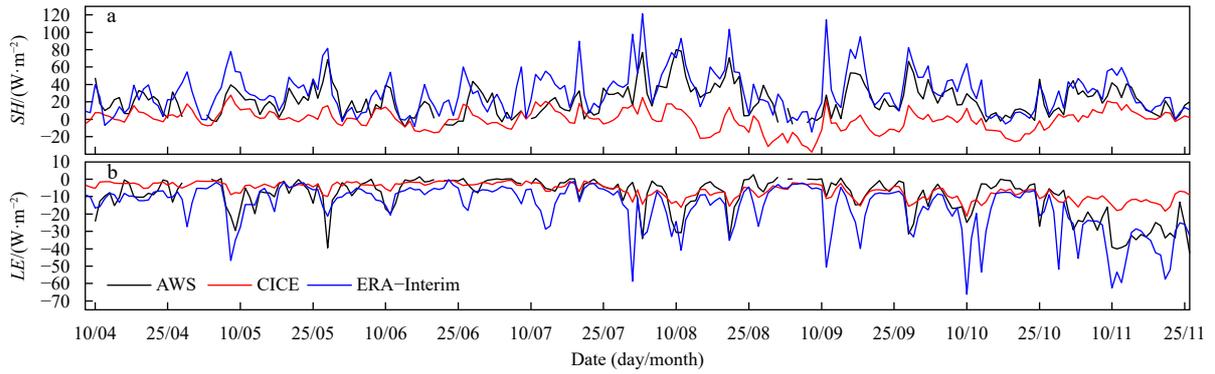
Fig. 5. Daily average *SH* (a) and *LE* (b). The sign convention is such that upward heat fluxes are positive and downward heat fluxes are negative.
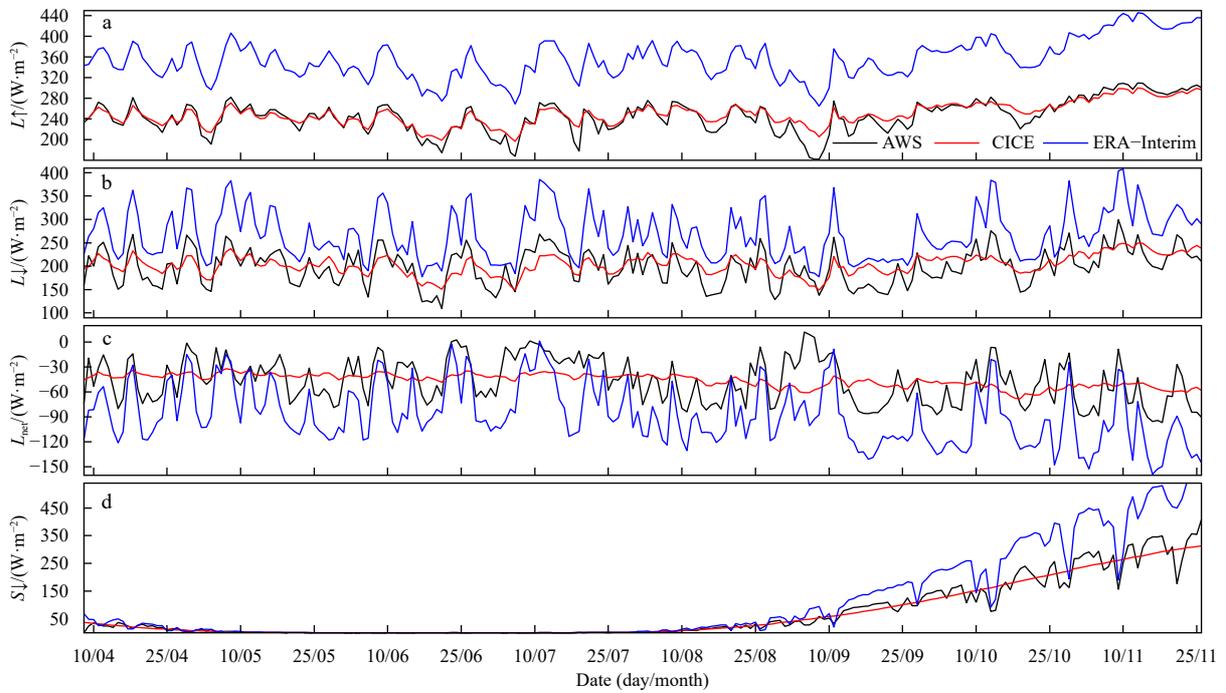
Fig. 6. Daily average upward longwave radiation (a), downward longwave radiation (b), net longwave radiation (c), and downward shortwave radiation (d).
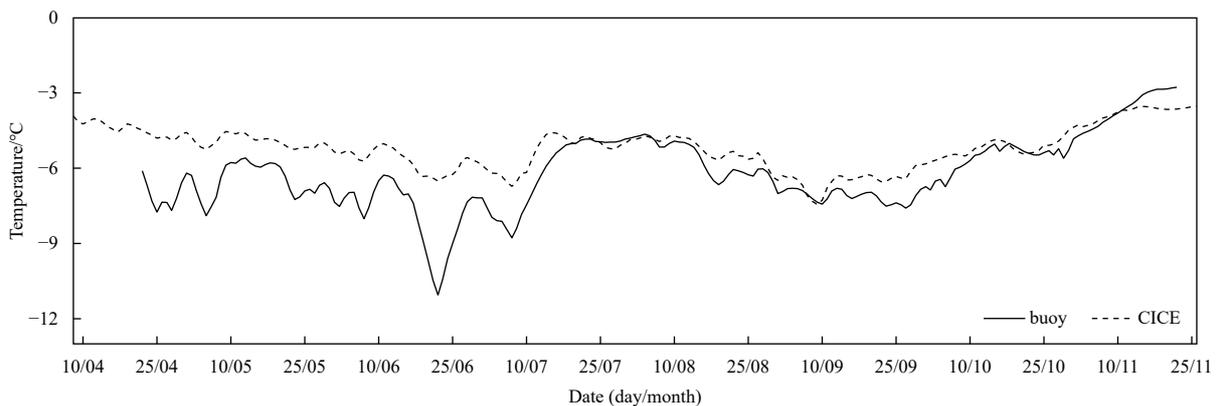
Fig. 7. Daily average ice temperature of buoy and CICE.

fluctuation from day to day. The simulated ice temperature was assessed with respect to the temperature observed by ice buoys. The ice temperature (Fig. 7) from CICE was reported in seven levels for five different ice categories, which were averaged and then compared with the observations. The bias and MAE were 0.9°C and 1.0°C, respectively. The simulated ice temperature also showed the temperature increase process from September. The simulated ice temperature can also demonstrate rapidly decreasing processes caused by the air temperature decrease, such as the process around 22 June and 7 July, but did not show the amplitude.

4 Discussion and conclusions

This study analyzed the flux variation, evaluated the reanalysis datasets and the CICE results based on the *in situ* data observed on landfast ice nearby the Zhongshan Station from 8 April to 26 November 2016. According to the results of Liu et al. (2020), the *in situ* data demonstrated that the strong katabatic wind enhanced the downward *SH* in Antarctica and the downward radiation, with significant differences in the monthly mean diurnal variation and demonstrated that *LE* was the only heat sink of the surface. In this study, the daily average turbulence flux and F_W were briefly analyzed. The reanalysis data and CICE 6 output results were evaluated by using the *in situ* data. The reanalysis data showed large differences compared with the observation data, The CICE 6 output of *SH*, *LE*, and the longwave radiation also showed larger errors and still needs to be improved.

The solar radiation demonstrated both seasonal and inner-seasonal variation, which was mainly caused by the solar elevation angle variation and the temperature impact by the synoptic process. In this study, the *SH* and L_{net} showed remarkable variation as mentioned above. The ice surface lost energy mainly through the outgoing longwave radiation from the middle of October. The ice-ocean energy also demonstrated seasonal variation. In this result, the ice growth rate varied between 0 and –0.3 m/d, which showed slight melt in the middle of November and similar with the 0–1.7 cm/d show in Lei et al. (2010). The calculated F_W demonstrated seasonal change with a range of 19–23 W/m² and 8–13 W/m² before and after August, respectfully; and the averaged F_W was 21 W/m² and 11 W/m² for these two periods, respectively. The F_W was dependent on the growth rate of ice, which can induce larger errors. The result of F_W was consistent with the previous experiment (Lei et al., 2010; Zhao et al., 2019), but show different seasonal variation, which may cause by the errors of sea ice grow rate in different seasons.

By choosing the nearest grid with the *in situ* site, the reanalysis data from NCEP R2, ERA-Interim, and JRA55 were evaluated. The comparison results show that the JRA55 dataset demonstrate the smallest bias and MAE with the observation data. The bias and MAE of *SH* were 0.7 W/m² and 6.8 W/m² and those of *LE* were –1.1 W/m² and 13.5 W/m². The NCEP R2 data show the largest difference with the observation data. The bias and MAE of *SH* were –7.9 W/m² and 11.3 W/m², and those of *LE* were 26.1 W/m² and 39.3 W/m². The ERA-Interim data show moderate differences for the *SH* and *LE*. The bias and MAE of *SH* were –6.5 W/m² and 7.6 W/m²and those of *LE* were 10.2 W/m² and 14.3 W/m², although it has the highest spatial regulation. The *SH* and *LE* for the ERA-Interim were presented by the forecasted element, which also induced more errors.

The CICE results were forced by the ERA-Interim atmospheric data. The radiation was simulated by CICE by using the ERA-Interim forcing data. The radiation results were consistent with the observed data, but did not demonstrate the amplitude of in

ner seasonal variation, with *SH* bias and MAE of –21.4 W/m² and 22.3 W/m², and *LE* bias and MAE of 3.1 W/m² and 5.9 W/m². These turbulent heat fluxes from CICE output were better than the NCEP R2 results compared with the *in situ* results and showed larger differences with the ERA-Interim data. The radiations (upward longwave radiation, downward longwave radiation, downward shortwave radiation) stimulated by CICE based on ERA-Interim data were better than the results of ERA-Interim. The averaged sea ice temperature can show the rapidly decreasing process caused by air temperature decreasing, such as the temperature decrease fall period in June and July, the local minimum temperature occurred on 22 June, and 7 July, and the temperature increase period from September. However, the amplitude was largely different, but was close to the observation result from the buoys, with bias and MAE of 0.9°C and 1.0°C, respectively.

The variation of surface flux on sea ice was briefly analyzed, and the model results were evaluated in this study. However, the observations were limited to the landfast ice site near the Zhongshan station. More observations are needed to cover a wider ice range and time scales to understand the surface energy balance, evaluate the model results, and improve the parameterization scheme. The results from this study also indicated that the JRA55 can be the forcing data used in CICE in the future.

References

Allison I, Tivendale C M, Akerman G J, et al. 1982. Seasonal variations in the surface energy exchanges over antarctic sea ice and coastal waters. Annals of Glaciology, 3: 12–16, doi: 10.1017/S0260305500002445

Bintanja R, Van Den Broeke M R. 1995. The surface energy balance of antarctic snow and blue ice. Journal of Applied Meteorology, 34(4): 902–926, doi: 10.1175/1520-0450(1995)034<0902:TSEBOA>2.0.CO;2

Blanken P D, Rouse W R, Culf A D, et al. 2000. Eddy covariance measurements of evaporation from Great Slave Lake, Northwest Territories, Canada. Water Resources Research, 36(4): 1069–1078, doi: 10.1029/1999WR900338

Comiso J C, Gersten R A, Stock L V, et al. 2017. Positive trend in the Antarctic sea ice cover and associated changes in surface temperature. Journal of Climate, 30(6): 2251–2267, doi: 10.1175/JCLI-D-16-0408.1

Ding Minghu, Agrawal A, Heil P, et al. 2019. Surface energy balance on the Antarctic plateau as measured with an automatic weather station during 2014. Advances in Polar Science, 30(2): 93–105, doi: 10.13679/j.advps.2018.0050

Ebita A, Kobayashi S, Ota Y, et al. 2011. The Japanese 55-year reanalysis "JRA-55": an interim report. Scientific Online Letters on the Atmosphere: SOLA, 7(1): 149–152, doi: 10.2151/sola.2011-038

Elders A, Pegion K. 2017. Diagnosing sea ice from the North American multi model ensemble and implications on mid-latitude winter climate. Climate Dynamics, 53(12): 7237–7250, doi:

10.1007/s00382-017-4049-3

Hao Guanghua, Pirazzini R, Yang Q, et al. 2020. Spectral albedo of coastal landfast sea ice in Prydz Bay. Antarctica. Journal of Glaciology, 67(261): 1–11, doi: 10.1017/jog.2020.90

Hunke E, Richard A, David A, et al. 2018. CICE-Consortium/CICE Version 6.0.0.alpha. Los Alamos, NM, USA: Los Alamos National Laboratory, doi: 10.5281/zenodo.1205675

Kanamitsu M, Ebisuzaki W, Woollen J, et al. 2002. NCEP–DOE AMIP-II Reanalysis (R-2). Bulletin of the American Meteorological Society, 83(11): 1631–1644, doi: 10.1175/BAMS-83-11-1631

King J C, Connolley W M, Derbyshire S H. 2001. Sensitivity of modelled Antarctic climate to surface and boundary-layer flux parametrizations. Quarterly Journal of the Royal Meteorological Society, 127(573): 779–794, doi: 10.1002/qj.49712757304

King J C, Gadian A, Kirchgaessner A, et al. 2015. Validation of the summertime surface energy budget of Larsen C Ice Shelf (Antarctica) as represented in three high-resolution atmospheric models. Journal of Geophysical Research: Atmospheres, 120(4): 1335–1347, doi: 10.1002/2014JD022604

Lei Ruibo, Li Zhijun, Cheng Bin, et al. 2010. Annual cycle of landfast sea ice in Prydz Bay, east Antarctica. Journal of Geophysical Research: Oceans, 115(C2): C02006, doi: 10.1029/2008JC005223

Liu Changwei, Gao Zhiqiu, Yang Qinghua, et al. 2020. Measurements of turbulence transfer in the near-surface layer over the Antarctic sea-ice surface from April through November in 2016. Annals of Glaciology, 62(82): 12–23, doi: 10.1017/aog.2019.48

McPhee M G, Untersteiner N. 1982. Using sea ice to measure vertical heat flux in the ocean. Journal of Geophysical Research: Oceans, 87(C3): 2071–2074, doi: 10.1029/JC087iC03p02071

Perovich D K, Elder B. 2002. Estimates of ocean heat flux at SHEBA. Geophysical Research Letters, 29(9): 58-1–58-4, doi: 10.1029/2001GL014171

Perovich D K, Grenfell T C, Light B, et al. 2002. Seasonal evolution of the albedo of multiyear Arctic sea ice. Journal of Geophysical Research: Oceans, 107(C10): SHE 20-1–SHE 20-13, doi: 10.1029/2000JC000438

Perovich D K, Polashenski C. 2012. Albedo evolution of seasonal Arctic sea ice. Geophysical Research Letters, 39(8): L08501, doi: 10.1029/2012GL051432

Persson P O G, Fairall C W, Andreas E L, et al. 2002. Measurements near the Atmospheric Surface Flux Group tower at SHEBA: Near-surface conditions and surface energy budget. Journal of Geophysical Research: Oceans, 107(C10): SHE 21-1–SHE 21-35, doi: 10.1029/2000JC000705

Shu Qi, Qiao Fangli, Song Zhenya, et al. 2012. Sea ice trends in the Antarctic and their relationship to surface air temperature during 1979–2009. Climate Dynamics, 38(11): 2355–2363, doi:

10.1007/s00382-011-1143-9

Simmons A, Uppala S, Dee D, et al. 2007. ERA-Interim: New ECMWF reanalysis products from 1989 onwards. ECMWF Newsletter, 110: 25–35

Välisuo I, Vihma T, King J C. 2014. Surface energy budget on Larsen and Wilkins ice shelves in the Antarctic Peninsula: results based on reanalyses in 1989–2010. The Cryosphere, 8(4): 1519–1538, doi: 10.5194/tc-8-1519-2014

Valkonen T, Vihma T, Doble M. 2008. Mesoscale modeling of the atmosphere over Antarctic sea ice: a late-autumn case study. Monthly Weather Review, 136(4): 1457–1474, doi: 10.1175/2007MWR2242.1

Van Den Broeke M R, Reijmer C, Van As D, et al. 2005. Seasonal cycles of Antarctic surface energy balance from automatic weather stations. Annals of Glaciology, 41(1): 131–139, doi: 10.3189/172756405781813168

Vihma T, Johansson M M, Launiainen J. 2009. Radiative and turbulent surface heat fluxes over sea ice in the western Weddell Sea in early summer. Journal of Geophysical Research: Oceans, 114(C4): C04019, doi: 10.1029/2008JC004995

Walden V P, Hudson S R, Cohen L, et al. 2017. Atmospheric components of the surface energy budget over young sea ice: Results from the N-ICE2015 campaign. Journal of Geophysical Research: Atmospheres, 122(16): 8427–8446, doi: 10.1002/2016JD026091

Wendler G, Adolphs U, Hauser A, et al. 1997. On the surface energy budget of sea ice. Journal of Glaciology, 43(143): 122–130, doi: 10.3189/S0022143000002884

Wendler G, Worby A P. 2001. The surface energy budget in the Antarctic summer sea-ice pack. Annals of Glaciology, 33: 275–279, doi: 10.3189/172756401781818220

Yang Qinghua, Liu Jiping, Leppäranta M, et al. 2016. Albedo of coastal landfast sea ice in Prydz Bay, Antarctica: Observations and parameterization. Advances in Atmospheric Sciences, 33(5): 535–543, doi: 10.1007/s00376-015-5114-7

Yu Lejiang, Yang Qinghua, Zhou Mingyu, et al. 2017. The variability of surface radiation fluxes over landfast sea ice near Zhongshan station, east Antarctica during austral spring. International Journal of Digital Earth, 12(8): 860–877, doi: 10.1080/17538947.2017.1304458

Zhao Jiechen, Yang Qinghua, Cheng Bin, et al. 2019. Spatial and temporal evolution of landfast ice near Zhongshan Station, East Antarctica, over an annual cycle in 2011/2012. Acta Oceanologica Sinica, 38(5): 51–61, doi: 10.1007/s13131-018-1339-5

Zhou Chunlüe, Wang Kaicun. 2016. Evaluation of surface fluxes in ERA-Interim using flux tower data. Journal of Climate, 29(4): 1573–1582, doi: 10.1175/JCLI-D-15-0523.1